12-2017

Vertically-aligned Mn(OH)2 nanosheet films for flexible all-solid-state electrochemical supercapacitors

Ziyuan Yang
Hohai University

Jiangfeng Gong
Hohai University

Chunmei Tang
Hohai University

Weihua Zhu
Hohai University

Zhaojun Cheng
Hohai University

See next page for additional authors

Vertically-aligned Mn(OH)2 nanosheet films for flexible all-solid-state electrochemical supercapacitors

Abstract
The arrangement of the electrode materials is a significant contributor for constructing high performance supercapacitor. Here, vertically-aligned Mn(OH)2 nanosheet thin films were synthesized by cathodic electrodeposition technique on flexible Au coated polyethylene terephthalate substrates. Morphologies, microstructures, chemical compositions and valence state of the nanosheet films were characterized systematically. It shows that the nanosheets arranged vertically to the substrate, forming a porous nanowall structures and creating large open framework, which greatly facilitate the adsorption or diffusion of electrolyte ions for faradaic redox reaction. Electrochemical tests of the films show the specific capacitance as high as 240.2 F g−1 at 1.0 A g−1. The films were employed to assemble symmetric all-solid-state supercapacitors with LiCl/PVA gel severed as solid electrolyte. The solid devices exhibit high volumetric capacitance of 39.3 mF cm−3 at the current density 0.3 mA cm−3 with robust cycling stability. The superior performance is attributed to the vertically-aligned configuration.

Disciplines
Materials Chemistry | Materials Science and Engineering | Nanoscience and Nanotechnology

Authors
Ziyuan Yang, Jiangfeng Gong, Chunmei Tang, Weihua Zhu, Zhaojun Cheng, Jinghua Jiang, Aibin Ma, and Qingping Ding

Vertically-aligned $Mn(OH)_2$ Nanosheet Films for Flexible All-solid-state Electrochemical Supercapacitors

Ziyuan Yang[1], Jiangfeng Gong [1,*], Chunmei Tang[1], Weihua Zhu[1], Zhaojun Cheng[2] Jinghua Jiang[2], Aibin Ma[2], Qingping Ding[3]

[1] College of Science, Hohai University, Nanjing 210098, P. R. China

[2] College of mechanics and materials, Hohai University, Nanjing 210098, P. R. China

[3] Ames Laboratory, US DOE, Ames, Iowa 50011, United States

* To whom correspondence should be addressed. E-mail: jfgong@hhu.edu.cn.

Abstract: The arrangement of the electrode materials is significant contributor for constructing high performance supercapacitor. Here, vertically-aligned $Mn(OH)_2$ nanosheet thin films were synthesized by cathodic electrodeposition technique on flexible Au coated polyethylene terephthalate substrates. Morphologies, microstructures, chemical compositions and valence state of the nanosheet films were characterized systematically. It is show that the nanosheets arranged vertically to the substrate, forming a porous nanowall structures and creating large open framework, which can greatly facilitate the adsorption or diffusion of electrolyte ions for faradaic redox reaction. Electrochemical tests of the films show the specific capacitance as high as 240.2 F g^{-1} at 1.0 A g^{-1}. The films were employed to assemble symmetric all-solid-state supercapacitors with LiCl/PVA gel severed as solid electrolyte. The solid devices exhibit high volumetric capacitance of 39.3 mF cm^{-3} at the current density 0.3 mA cm^{-3} with robust cycling stability. The superior performance can be attributed to the vertically-aligned configuration.

Key words: Manganese hydroxide; Electrodeposition; All-solid-state Supercapacitors; Flexibility.

Acknowledgments: This work was supported by the National Natural Science Foundation of China (No. 11104062), the Fundamental Research Funds for the Central Universities (Grant Nos. 2015B22313 and 2016B46014)

1. Introduction

As fast growing of consumer electronics market, the requirements of the energy storage have become increasingly diverse, such as flexibility, light weight and quick charging. All-solid-state (ASS) supercapacitors (SCs) have attracted much attention for energy storage, which show great advantages with high powder density and long cycle lifetime [1-3]. To develop an advanced ASS-SCs device, active electrode material with high capacity performance is indispensable.

Various electrode materials had been developed in the past decade. Based on the energy storage mechanism, they can be classified into two categories. One is electric double layer based capacitors (EDLC), in which, the ions were absorbed at the interface between electrode materials and the electrolyte solution by external electrostatic forces. This kind of active materials (for example carbon-based materials) can offer high power density and excellent cycling ability，but suffer relative low capacitance compared with rechargeable batteries [4-8]. The other is faradaic pseudo-capacitor, the energy stored by reversible redox reactions take place at surfaces of the electrode materials. The representative electrode active material is RuO_2, which exhibit much higher specific capacitance than conventional carbon materials [9-11]. For example, Dubal D. P. et.al. reported that the highest specific capacitance of RuO_2 thin films can reach 243 F g^{-1} [11]. However, the high cost limits it for commercialization. Therefore, the development of inexpensive alternative electrode materials with high performance has been one of the hottest research topics. Transition metal oxides and hydroxides such as MnO_2, $Mn(OH)_2$ were widely investigated as pseudo-capacitive electrode materials in recent years because of their low cost, environmentally friendly, and excellent capacitive performance [12-16]. Among them, manganese oxides were widely studied, while few reports referred to $Mn(OH)_2$.

In this work, vertically-aligned $Mn(OH)_2$ nanosheet films were synthesized by cathodic electrodeposition technique. The nanosheets crossed each other and formed much micro-pore at their border, which avoided the stacking of $Mn(OH)_2$ nanosheets and fully utilized the surfaces and edges for faradaic redox reaction, and provided open channels that led to the efficient diffusion of ions. Due to its specific configuration, the $Mn(OH)_2$ nanosheet films exhibit improved electrochemical performance with a specific capacitance as high as 240.2 F g^{-1} at 1.0 A g^{-1} at three electrode mode using 1 M Na_2SO_4 as electrolyte, which is much higher than that of carbon based materials, and comparable to reported transition metal oxides [11, 17]. Because of its high specific capacitance, the films were employed to assemble symmetric ASS-SCs with LiCl/PVA gel severed as solid electrolyte. The assembled device exhibit high volumetric capacitance (39.3 mF cm^{-3}) at the current density 0.3 mA cm^{-3}. In addition, the ASS-SCs show robust cycling stability, the capacitance remained 95.3% of its original value after 10000 charge-discharge (CD) cycles.

2. Experimental section

2.1. Electrodeposition of $Mn(OH)_2$ Nanosheet Films

The electrodeposition was carried out in a three-electrode system. Gold coated Polyethylene terephthalate (PET), platinum plate, and saturated calomel electrode (SCE) were used as working electrode, counter electrode and reference electrode, respectively. All deposition potentials are reported with respect to this reference. The electrolyte solution consisted of 0.1 M $Mn(CH_3COO)_2$ and 0.1 M KNO_3 without adjusting its pH value. The deposition potentials were investigated systematically. After the electrodeposition, the films were rinsed with distilled water and dried at room temperature in air.

2.2. Materials Characterization

The morphologies and the microstructures were characterized using scanning electron microscopy (SEM, Quanta 200, FEI) and transmission electron microscopy (TEM, Tecnai F20, FEI) equipped with an energy-dispersive X-ray spectrometer (EDS, EDAX Co.). The elemental compositions were analyzed by an X-ray photoelectron spectroscopy (XPS, ESCALAB 250 Xi, Thermo Fisher Scientific).

2.3. Electrochemical Measurement

Cyclic voltammetry (CV), galvanostatic charge-discharge (GCD) and electrochemical impedance spectroscopy (EIS) of $Mn(OH)_2$ films were evaluated on the electrochemical workstation (CHI 660D, Chenhua Co. Shanghai). In the three-electrode mode, $Mn(OH)_2$/Au/PET (1 cm^2) were used as working electrode, platinum plate, and SCE were used as counter electrode and reference electrode, respectively. The electrolyte used was 1 M Na_2SO_4 aqueous solution. The ASS-SCs were examined in the two-electrode mode using PVA/LiCl gel as electrolyte. The electrolyte was prepared as follow: 6 g of LiCl was added into 60 mL of deionized water, and then 6 g of PVA power was added. The whole mixture was heated to 85 °C under stirring until the solution became clear. Two pieces of $Mn(OH)_2$/Au/PET electrodes were immersed in the PVA/LiCl gel solution for 5 min to adsorb a layer of solid electrolyte. Then they were pressed together and dried at 50 °C in an oven for 24 h.

3. Results and discussion

3.1. Structure and morphology

In the experiments, it was found that deposition potential is the most important parameter on the composition and morphology of deposited products. In order to investigate the morphology evolution

along with the deposition potentials, samples obtained at different deposition potentials were shown in **Fig. 1**. It is clearly that only agglomerated $Mn(OH)_2$ nanoparticles were observed at -0.9 V (vs. SCE) (**Fig. 1a**). With increasing deposition potential to -1.0 V (vs. SCE), the nanoparticles were assemble into nanosheets as shown in **Fig. 1b**. When the deposition potential increased to -1.1 or -1.15 V (vs. SCE), the products exhibit a highly porous structure made up of interconnected $Mn(OH)_2$ nanosheet arrays (**Fig. 1c and d**). Apparently, the nanosheets arranged vertically to the substrate, forming a porous nanowall structures and creating large open framework. The pores between the $Mn(OH)_2$ nanoshees have a diameter ranging from dozens of nanometers to a few micrometers. It is reported that the macro-pores configuration of electrode materials can greatly facilitate the adsorption or diffusion of electrolyte ions for faradaic redox reaction [18-20]. Here, the synthesized $Mn(OH)_2$ nanosheet films show the similar configuration, which were expected to have enhanced electrochemical property. When the deposition potential is more negative than -1.15 V(vs. SCE), some bubbles arise from the cathodic substrate, which would making the $Mn(OH)_2$ films slipped off from the substrate. Here we use $Mn(OH)_2$ films deposited at -1.15 V(vs. SCE) to build ASS-SCs and evaluate its electrochemical property.

The microstructures of the $Mn(OH)_2$ nanosheets were further investigated by TEM. Due to its interpenetrating configuration, it is hard to exfoliate to form single nanosheets with ultrasonic treatment. **Fig. 2a** shows typical TEM image of the intertwined $Mn(OH)_2$ nanosheets, the thickness of the film was estimated to be about 4μm. The corresponding selected area electron diffraction (SAED) is shown in **Fig. 2b,** the well-defined diffraction rings indicated its polycrystalline characterization. The calculated d-spacings are 0.29 nm, 0.25 nm, 0.18 nm, 0.17 nm, 0.14 nm, 0.12 nm and 0.11 nm which

close to the interplanar of (100), (011), (012), (110), (103), (202) and (104) planes of $Mn(OH)_2$ (JCPDS no. 73-1604). High-resolution TEM image in **Fig. 2c** exhibits clearly crystal lattice, the measured lattice spacing is 0.25 nm, which corresponding to (011) interplanar separation of $Mn(OH)_2$ (JCPDS no. 73-1604), confirming its crystalline nature in consistent with the SAED results. EDX spectroscopy in **Fig. 2d** demonstrates that the Mn and O, can be detected in the nanosheet (signals of C and Cu come from the TEM copper grid). By integration calculation, the atomic ratio of Mn and O are 33:67, which is close to 1:2, implying that the nanosheet may be $Mn(OH)_2$.

XPS was conducted in order to better understand the composition and oxidation state of the $Mn(OH)_2$ films as shown in **Fig 3**, the cycles represent the measured data and the solid lines indicate fitted curves. **Fig. 3a** shows the high-resolution Mn 2p spectrum, where two peaks located at 642.0 and 653.8 eV can be attributed to Mn $2p_{3/2}$ and Mn $2p_{1/2}$, respectively. However, it is difficult to discriminate the valence state of Mn unambiguously due to some differential charging raised by the ejection of photoelectrons [21]. **Fig. 3b** exhibits the O 1s spectrum, which can be de-convoluted into two components, suggesting the presence of two types of oxygen-containing species. The peak located at 531.6 eV is assigned to the oxygen bond of Mn-OH, while the band at 530.1 eV corresponds to Mn-O-Mn [21-23]. In addition with the TEM and EDX results above, it can be concluded the composition can be identified as $Mn(OH)_2$.

3.2. Electrochemical properties

The electrochemical performance of the $Mn(OH)_2$ nanosheet films were examined using 1.0 M Na_2SO_4 electrolyte. **Fig. 4a** shows the CV curves of the Au/PET substrate and the $Mn(OH)_2$ nanosheet

film at a scan rate of 200 mV s^{-1} in a potential window of -0.2 to 0.8 V *vs* SCE. The integrated CV area of the Au/PET substrate is much lower than that of $Mn(OH)_2$ nanosheet film, this illustrates that the contribution of substrate to the total electrochemical capacitance can be neglected. **Fig. 4b** shows the CV curves of $Mn(OH)_2$ electrode at scan rates from 10 to 200 mV s^{-1}, which exhibited rectangular shape at low scan rates, indicative of the pseudo-capacitive nature of the electrode [17, 24]. With increasing the scan rate, the shape of the CV curves were slightly deviated from rectangular shape, this probably caused by ion transplant during the charge process, from which the ions can only reach the surface of the electrode and not enter the inside of the electrode at a high scan rate [17]. **Fig. 4c** illustrates the GCD curves of $Mn(OH)_2$ electrode at different current densities from 1.0 to 6.7 A g^{-1}. The calculated specific capacitances are presented in **Fig. 4d**. A highest specific capacitance of 240.2 F g^{-1} was obtained at 1.0 A g^{-1}, which is much higher than that reported ($Mn(OH)_2$, 147.4 F g^{-1}) by Yan et. al. [17]. The higher specific capacitance was attributed to its vertically-aligned configuration, the micro-pores offering many open channels for the diffusion of electrolyte ions to electrode surface, which inhibit the re-stacking of $Mn(OH)_2$ nanosheets and fully utilize their surfaces, thus enhanced its electrochemical property.

To further explore the feasibility of vertically-aligned $Mn(OH)_2$ nanosheets electrodes, Symmetric ASS-SCs were assembled using LiCl/PVA gel as the solid electrolyte. The schematic construction and the digital photograph of the ASS-SCs are shown in **Fig. 5a**. Because the films were deposited on thin Au/PET substrate, the thickness of the ASS-SC is only 0.035 cm and displayed excellent flexibility. **Fig. 5b** shows the CV curves of $Mn(OH)_2$ ASS-SCs at different scan rates. According to the CV studies of single electrode in **Fig. 4**, a potential window of 0 to 1.0 V applied. The CV curves still show good

rectangle shapes, indicating its pseudo-capacitive nature in ASS devices. **Fig. 5c** shows the GCD curves of the ASS-SCs device at different current densities from 0.3 to 1.4 mA cm^{-3}. The corresponding specific capacitances are exhibited in **Fig. 5d.** The highest volumetric capacitance of the $Mn(OH)_2$ ASS-SCs achieved 39.3 mF cm^{-3} at 0.3 mA cm^{-3}. The obtained maximum volumetric capacitance was higher than that of previously reported SC devices, such as carbon fiber-reinforced poly based device (10.3 mF cm^{-3}) [25], MoS2/rGO based SCs(6.56 mF cm^{-3}) [26], vanadium nitride nanosheets based ASS-SCs (1.937 mF cm^{-3}) [27]. These results confirmed that the vertically-aligned $Mn(OH)_2$ nanosheet films were promising active electrode materials for ASS-SCs devices. **Fig. 5e** shows the EIS spectrum of the ASS-SCs with a fitted equivalent circuit (inert), R_s, R_{ct}, C_p and CPE were calculated using the ZSimpWin software. R_s represent the combination of ionic resistance of electrolyte, intrinsic resistance of electrode material and interfacial resistances. R_{ct} offers information of charge transfer resistance relates to the radius of the semicircle. The low R_s and R_{ct} values of ASS-SC device (9.82 + 2.85) demonstrate its high electronic conductivity and electrochemical reactivity. The slope of the straight line larger than 45° in the low frequency region indicates the excellent capacitive behavior of the electrodes [28-30]. Cycle stability of the ASS-SCs were performed by GCD tests at the current density of 0.3 mA cm^{-3}, the GCD curves of the first and last 5cycles inserted in **Fig. 5f** show subtle changes and the capacitance retention reaches 95.3% of its initial value after 10000 cycles, indicating the excellent cycle stability.

In addition, considering its application in portable or wearable electronics, it is significantly important that the SCs device have good mechanical flexibility without losing its electrochemical performance. To demonstrate the mechanical flexibility of $Mn(OH)_2$ nanosheet films based SC, CV

measurement of the device at different bending angles (0°, 60°, 120° and 180°) was conducted at a scan rate of 200 mV s^{-1} **(Fig. 6a),** the bending angle was defined as shown in **Fig. 6b**. It is interesting to note that, CV curves of device show similar capacitive behavior with no obvious capacitance decay at different bending angles, suggesting the excellent adhesion of active electrode material with current collector and good quality of interface between the gel electrolyte and active electrode material.

4. Conclusions

In conclusion, vertically-aligned $Mn(OH)_2$ nanosheet films with open framework were synthesized by cathodic electrodeposition technique. Electrochemical tests of the films show the specific capacitance as high as 240.2 F g^{-1} at 1.0 Ag^{-1} at three electrode mode using 1 M Na_2SO_4 as electrolyte. The assembled ASS-SCs devices exhibit high volumetric capacitance (39.3 mF cm^{-3}) at the current density 0.3 mA cm^{-3} and show robust cycling stability, the capacitance remained 95.3% of its original value after 10000 charge-discharge cycles.

Reference:

1. P. Yang and W. Mai, Nano Energy **8**, 274-290 (2014).

2. D. Yu, K. Goh, H. Wang, L. Wei, W. Jiang, Q. Zhang, L. Dai and Y. Chen, Nat. Nanotechnol. **9**, 555-562 (2014).

3. X. Lu, M. Yu, G. Wang, Y. Tong and Y. Li, Energ. Environ. Sci. **7**, 2160-2181 (2014).

4. J. Chmiola, C. Largeot, P.-L. Taberna, P. Simon and Y. Gogotsi, Science **328**, 480-483 (2010).

5. G. Wang, L. Zhang and J. Zhang, Chem. Soc. Rev. **41**, 797-828 (2012).

6. H. Jiang, P. S. Lee and C. Li, Energ. Environ. Sci. **6**, 41-53 (2013).

7. X. Zhang, J. Jin, P. Yan, J. Xu, R. Zhang and C. Wu, Mater. Lett. **160**, 190-193 (2015).

8. K. Jia, X. Zhuang, B. Cheng, S. Shi, Z. Shi and B. Zhang, J. Mater. Sci.-Mater. Electron. **24**, 4769-4773 (2013).

9. K.-M. Lin, K.-H. Chang, C.-C. Hu and Y.-Y. Li, Electrochim. Acta **54**, 4574-4581 (2009).

10. P. Wang, Y. Xu, H. Liu, Y. Chen, J. Yang and Q. Tan, Nano Energy **15**, 116-124 (2015).

11. D. P. Dubal, G. S. Gund, R. Holze, H. S. Jadhav, C. D. Lokhande and C.-J. Park, Electrochim. Acta **103**, 103-109 (2013).

12. X. Zhang, X. Meng, S. Gong, P. Li, L. e. Jin and Q. Cao, Mater. Lett. **179**, 73-77 (2016).

13. J. Yan, Q. Wang, T. Wei and Z. Fan, Adv. Energy Mater. **4**, 1300816 (2014).

14. B. Yin, S. Zhang, H. Jiang, F. Qu and X. Wu, J. Mater. Chem. A **3**, 5722-5729 (2015).

15. J. Zhu, S. Tang, H. Xie, Y. Dai and X. Meng, Acs Appl. Mater. Inter. **6**, 17637-17646 (2014).

16. Z. Li, Z. Liu, D. Li, B. Li, Q. Li, Y. Huang and H. Wang, J. Mater. Sci.-Mater. Electron. **26**, 353-359 (2015).

17. D. Yan, Y. Li, Y. Liu, R. Zhuo, Z. Wu, B. Geng, J. Wang, P. Ren, P. Yan and Z. Geng, Mater. Lett. **136**, 7-10 (2014).

18. J. Xiao, L. Wan, S. Yang, F. Xiao and S. Wang, Nano lett. **14**, 831-838 (2014).

19. N. Wang, P. Zhao, K. Liang, M. Yao, Y. Yang and W. Hu, Chem. Eng. J. **307**, 105-112 (2017).

20. L. Li, J. Gong, C. Liu, Y. Tian, M. Han, Q. Wang, X. Hong, Q. Ding, W. Zhu and J. Bao, ACS Omega **2**, 1089-1096 (2017).

21. W. Sun, A. Hsu and R. Chen, J. Power Sources **196**, 627-635 (2011).

22. H. W. Nesbitt and D. Banerjee, Am. Mineral. **83**, 305-315 (1998).

23. H. Fang, S. Zhang, X. Wu, W. Liu, B. Wen, Z. Du and T. Jiang, J. Power Sources **235**, 95-104 (2013).

24. S. Min, C. Zhao, Z. Zhang, K. Wang, G. Chen, X. Qian and Z. Guo, RSC Adv. **5**, 62571-62576 (2015).

25. A. Javaid, K. K. C. Ho, A. Bismarck, J. H. G. Steinke, M. S. P. Shaffer and E. S. Greenhalgh, J. Compos. Mater. **50**, 2155-2163 (2016).

26. Y. Xiao, L. Huang, Q. Zhang, S. Xu, Q. Chen and W. Shi, Appl.Phys. Lett. **107,** 013906 (2015).

27. W. Bi, Z. Hu, X. Li, C. Wu, J. Wu, Y. Wu and Y. Xie, Nano Res. **8**, 193-200 (2015).

28. K. Gao, Z. Shao, J. Li, X. Wang, X. Peng, W. Wang and F. Wang, J. Mater.Chem. A **1**, 63-67 (2013).

29. T. Chen, Y. Tang, Y. Qiao, Z. Liu, W. Guo, J. Song, S. Mu, S. Yu, Y. Zhao and F. Gao, Sci. Rep **6** 23289 (2016).

30. G. S. Gund, D. P. Dubal, N. R. Chodankar, J. Y. Cho, P. Gomez-Romero, C. Park and C. D.

Lokhande, Sci. Rep **5** 12454 (2015).

Figure Captions

Fig. 1 (a-d) SEM images of $Mn(OH)_2$ nanosheet films obtained at different deposition potentials: (a) -0.9 V(vs. SCE), (b) -1.0 V(vs. SCE), (c) -1.1 V(vs. SCE), (d) -1.15 V(vs. SCE)

Fig. 2 (a) TEM image, (b) SAED pattern，(c) HRTEM image and (d) EDX spectrum of the $Mn(OH)_2$ nanosheet films.

Fig. 3 XPS spectra of the $Mn(OH)_2$ nanosheet films. (a) Mn 2p, (b) O1s.

Fig. 4 (a) Comparative CV curves of the Au/PET substrate and $Mn(OH)_2$ electrode, (b) CV curves, (c) GCD curves and (d) the calculated specific capacitance of vertically-aligned $Mn(OH)_2$ nanosheets electrode.

Fig. 5 (a) Schematic and digital photograph, (b) CV curves, (c) GCD curves, (d) volume capacitance, (e) EIS curve and (f) Cycling performance of the flexible ASS-SCs. The inset shows the GCD curves of the first and last 5cycles.

Fig. 6 (a) Cyclic voltammetry curves and (b) digital photograph of the $Mn(OH)_2$ nanosheet films based ASS-SCs at different bending angles.

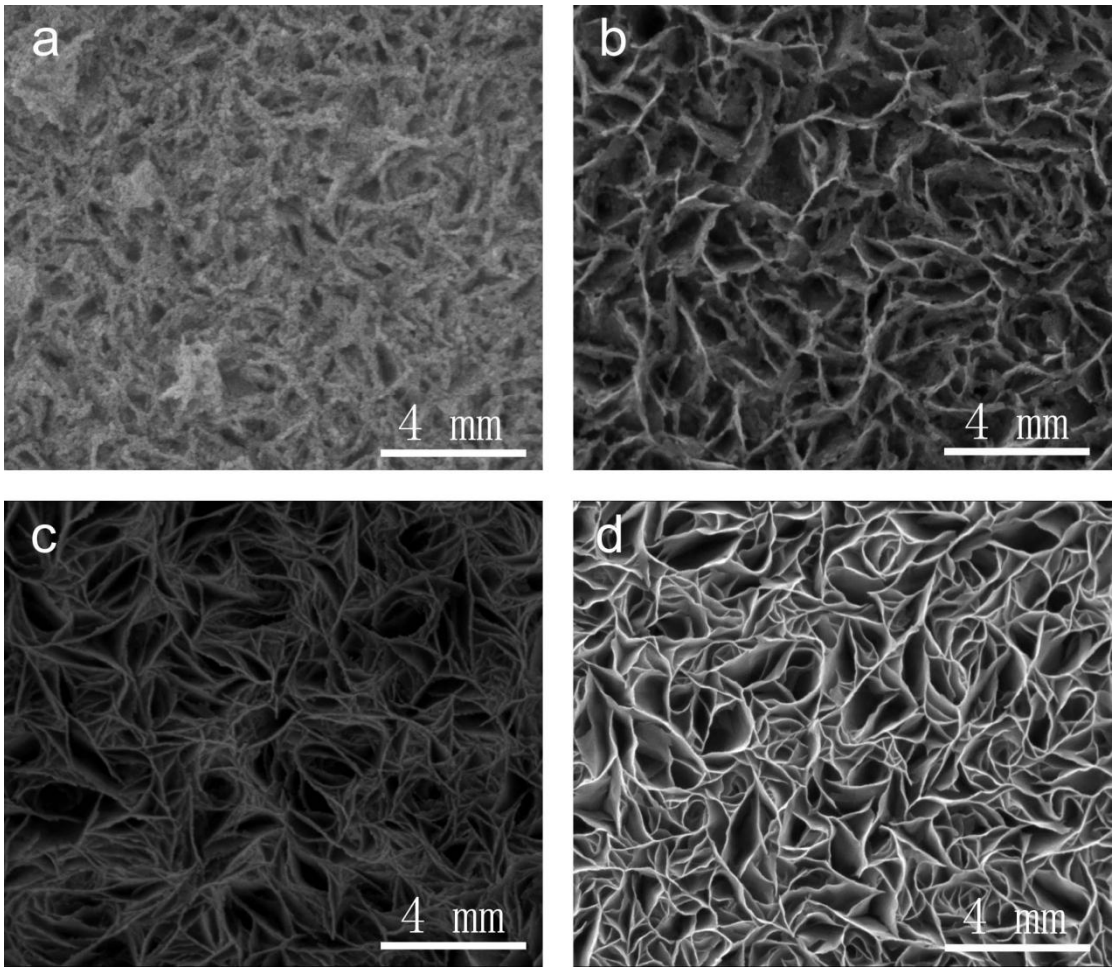

Figure 1.

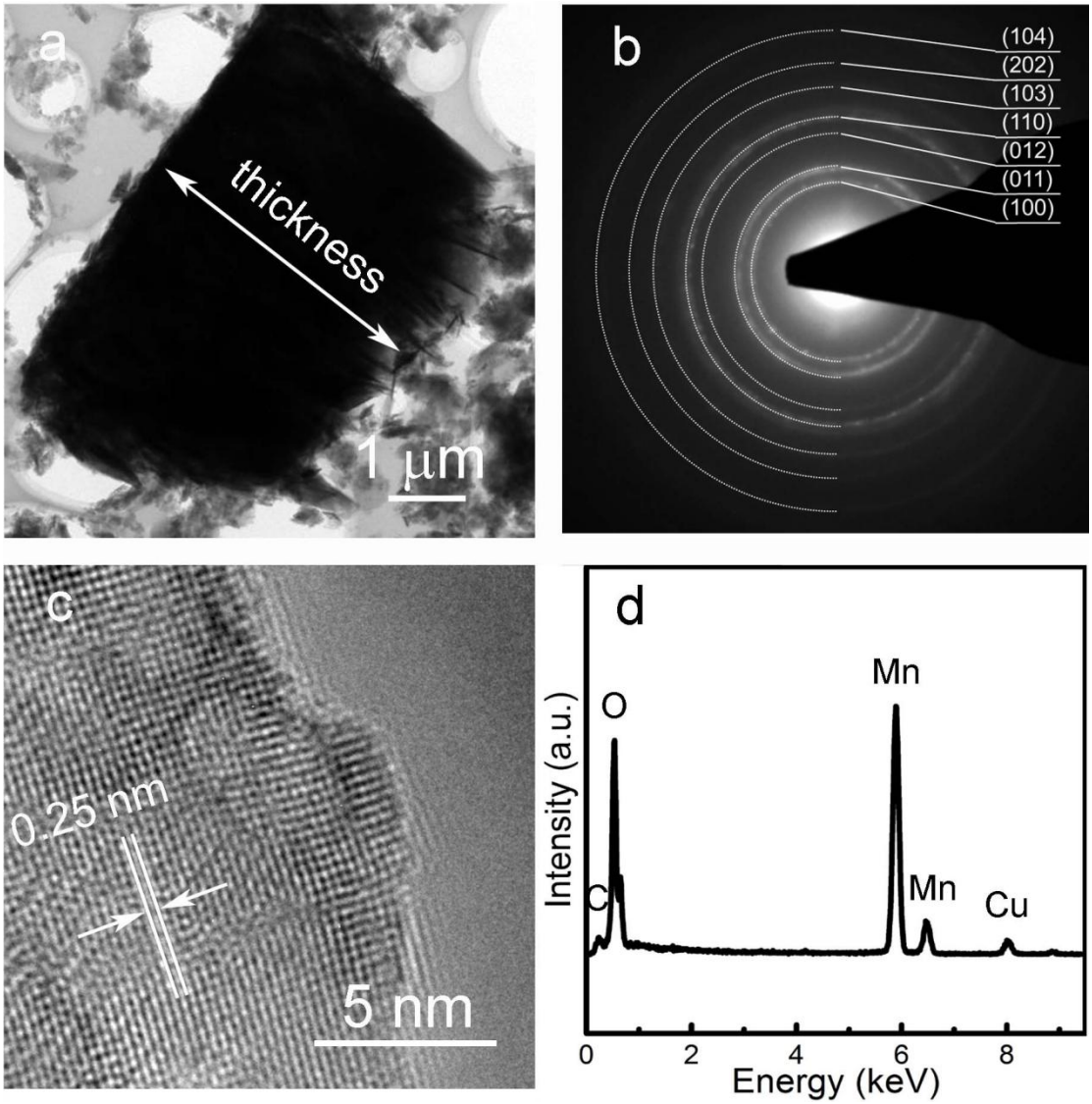
a
thickness
1 μm
b
(104)
(202)
(103)
(110)
(012)
(011)
(100)
c
0.25 nm
5 nm
d
Intensity (a.u.)
O
C
Mn
Mn
Cu
0
2
4
6
8
Energy (keV)

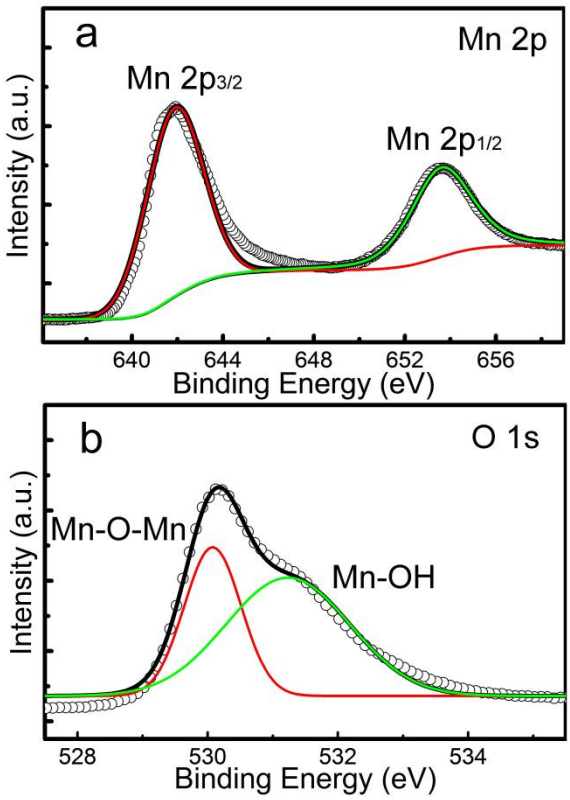

Figure 2.

Figure 3.

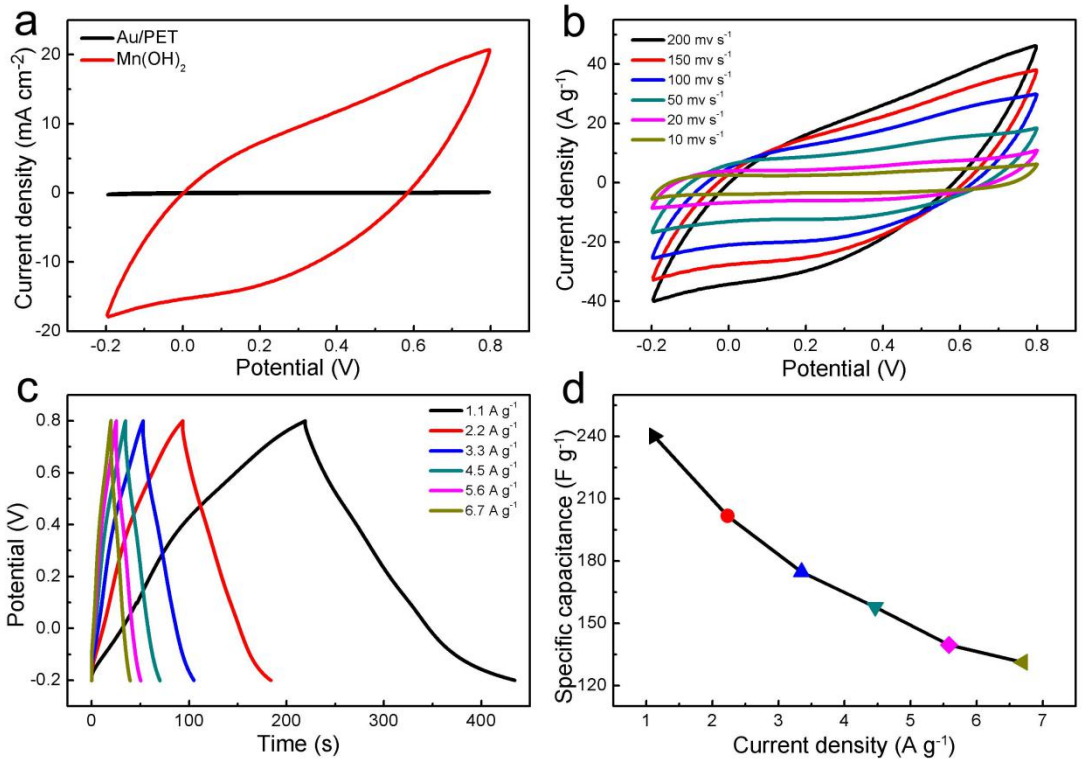
a
Au/PET
Mn(OH)2
Current density (mA cm-2)
Potential (V)
b
200 mv s-1
150 mv s-1
100 mv s-1
50 mv s-1
20 mv s-1
10 mv s-1
Current density (A g-1)
Potential (V)
c
1.1 A g-1
2.2 A g-1
3.3 A g-1
4.5 A g-1
5.6 A g-1
6.7 A g-1
Potential (V)
Time (s)
d
Specific capacitance (F g-1)
Current density (A g-1)

Figure 4.

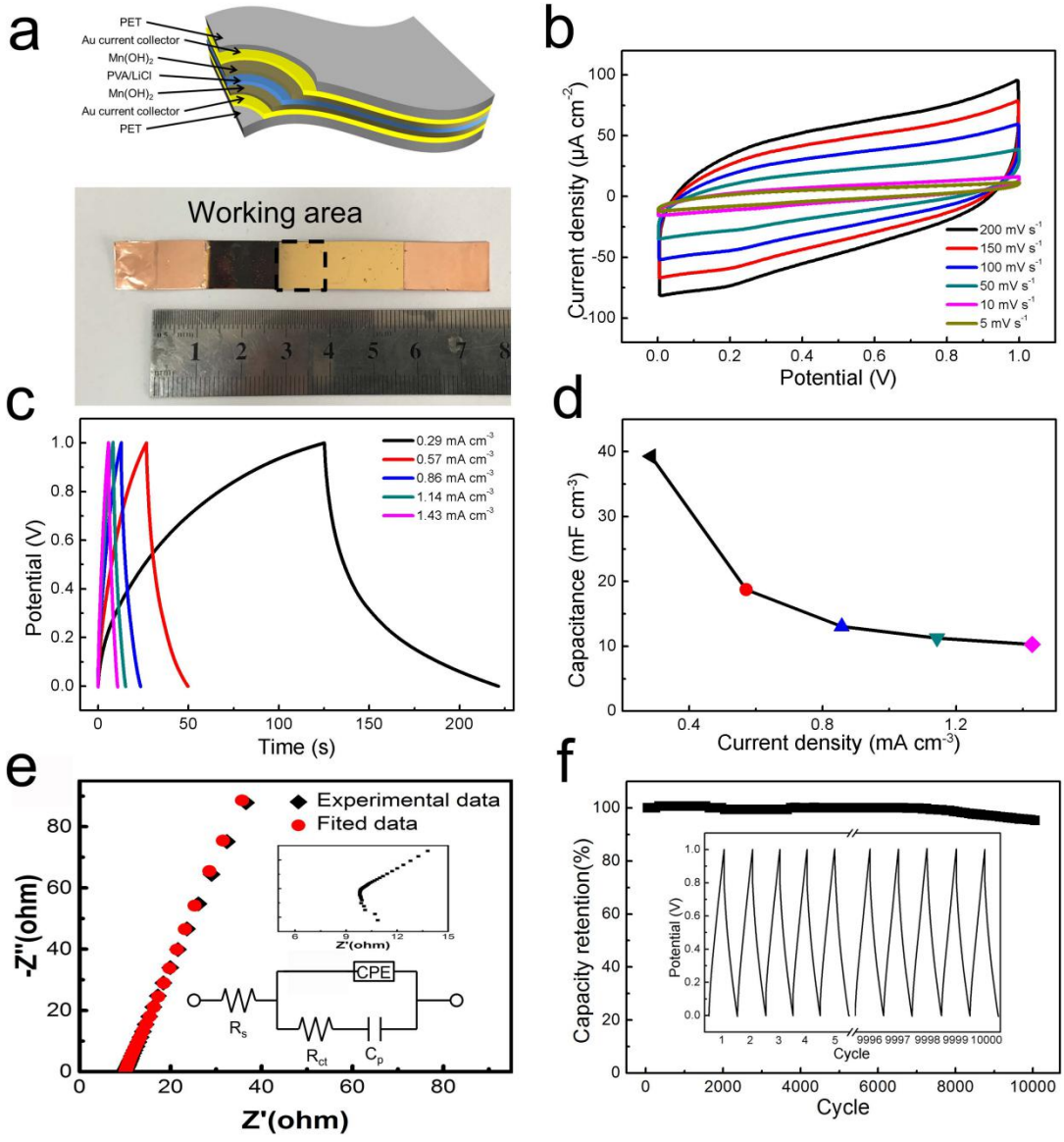
a
PET
Au current collector
Mn(OH)2
PVA/LiCl
Mn(OH)2
Au current collector
PET
Working area
b
Current density (μA cm-2)
Potential (V)
200 mV s-1
150 mV s-1
100 mV s-1
50 mV s-1
10 mV s-1
5 mV s-1
c
Potential (V)
Time (s)
0.29 mA cm-3
0.57 mA cm-3
0.86 mA cm-3
1.14 mA cm-3
1.43 mA cm-3
d
Capacitance (mF cm-3)
Current density (mA cm-3)
e
-Z''(ohm)
Z'(ohm)
Experimental data
Fited data
Z'(ohm)
CPE
Rs
Rct
Cp
f
Capacity retention(%)
Cycle
Potential (V)
Cycle

Figure 5.

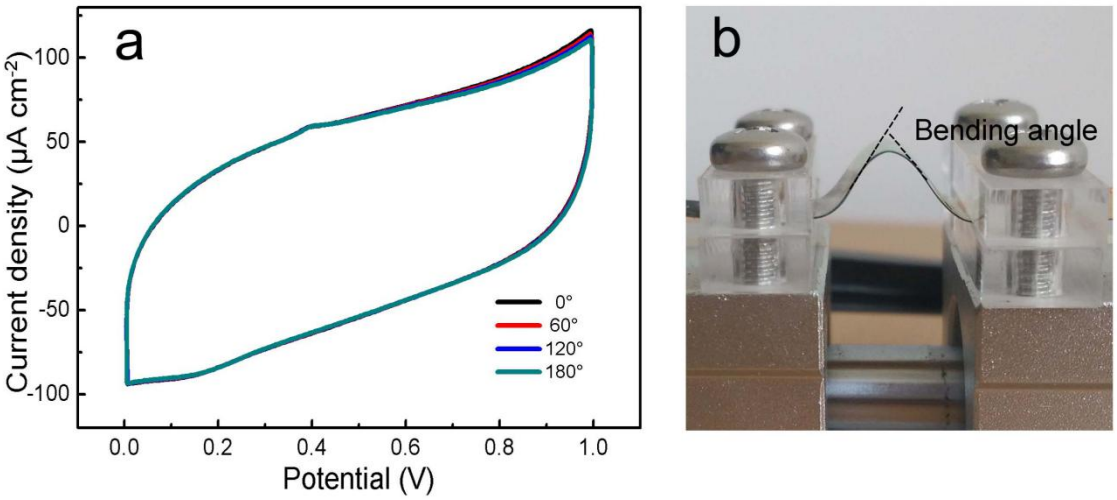
a
Current density (μA cm-2)
100
50
0
-50
-100
0.0
0.2
0.4
0.6
0.8
1.0
Potential (V)
0°
60°
120°
180°
b
Bending angle

Figure 6.